Hindawi
Structural Control and Health Monitoring
Volume 2023, Article ID 7743762, 19 pages
https://doi.org/10.1155/2023/7743762

Research Article

Feasibility of Accurate Point Cloud Model Reconstruction for Earthquake-Damaged Structures Using UAV-Based Photogrammetry

Jiazeng Shan,[1,2] **Hongtao Zhu**,[1] **and Runze Yu**[1]

[1]*Department of Disaster Mitigation for Structures, Tongji University, Shanghai, China*
[2]*Shanghai Engineering Research Center for Resilient Cities and Intelligent Disaster Mitigation, Shanghai, China*

Correspondence should be addressed to Runze Yu; 2110017@tongji.edu.cn

Received 22 November 2022; Revised 28 April 2023; Accepted 22 June 2023; Published 3 July 2023

Academic Editor: Young-Jin Cha

Camera-enabled unmanned aerial vehicles (UAVs) provide a promising technique to considerably speed up the inspection and visual data collection from regions that may otherwise be inaccessible. In addition, the technology of image-based 3D reconstruction can generate a point cloud model using images captured by UAVs. However, the performance of the point cloud modeling may be affected by multiple factors, such as the modeling software, ground control points (GCPs), and UAV flight modes. In this study, three common software packages were compared, and Pix4Dmapper was considered a suitable software for point cloud modeling for earthquake-damaged buildings. The accuracy and resolution of point cloud models are usually evaluated by root mean square error (RMSE) and ground sampling distance (GSD). The effects of the main factors, including the number of GCPs, distribution of GCPs, flight manner of the UAV, and distance from the UAV to the target, were investigated on the basis of two real-world multistory earthquake-damaged structures. The influence rules of the main factors revealed that a close range, automatic flight mode of the UAV, a large number of GCPs, and a relatively wide distribution of the GCPs may generate a point cloud model with low computational costs, high accuracy, and high resolution. In the particular illustration example here, the RMSE is 6.78 mm while the GSD is 1.60 mm. Finally, rapid structural damage inspection was demonstrated using an accurate point cloud model and compared with the inspection results of a total station and terrestrial laser scanner point cloud models. The comparison of different inspection results showed that the relative errors were relatively acceptable within 4%.

1. Introduction

Most buildings are becoming susceptible to losing their designed functions as they deteriorate from use. Once they experience earthquakes, buildings may lose more functions and become dangerous. This process signifies urgent maintenance and inspection issues. Because of this, many research groups have proposed computer vision-based structural health monitoring and structural damage inspection techniques [1–6]. For example, the vision-based method using a deep architecture of convolutional neural networks [1] and the faster region-based convolutional neural network-based structural visual inspection method [2] were proposed for detecting multiple types of damages in extensively varying situations. In addition, the unmanned aerial vehicle (UAV) surveying technology provides an efficient and convenient way to acquire visual information.

In recent years, UAVs have been widely applied in civil engineering [7]. With the rapid development of UAV technology [8], low-altitude UAV surveying and mapping technology provides a new efficient multidimensional information acquisition method for structural digitization [9], daily maintenance [10, 11], and postdisaster emergency assessment [12] of engineering structures. For example, the autonomous UAV system integrated with a modified faster region-based convolutional neural network was proposed to identify various types of structural damage and map the detected damage in a GPS-denied environment [13]. The autonomous UAV-based damage detection method using ultrasonic beacons was proposed for indoor environments

and areas in which GPS was denied or unreliable [14]. Therefore, UAVs play an important role in the entire life cycle of engineering structures. The daily maintenance of various structures, such as dams [15], bridges [16], roads [17], and buildings [18], can be realized by UAVs, which collect visual data from inaccessible regions [19]. In addition, UAVs can accomplish faster structural damage inspection and assessment in disaster areas because of the inconvenience of traffic after an emergency [20]. Structural digitization is the basis of daily maintenance and post-disaster emergency assessment [21–25], and image-based 3D reconstruction using images captured by UAVs is one of the prominent techniques for digitization of engineering structures [26].

Some studies have investigated the accuracy of the point cloud model of image-based 3D reconstruction. Because the different flight parameter combinations of UAVs have an important impact on the accuracy of the point cloud model [27], an appropriate flight and image capture strategy adequate to the quality requirements of the modeling can save time and resources [28]. The UAV observations obtained under different light conditions can be evaluated using terrestrial laser scanner acquisitions, which show the effect of light conditions on the accuracy of the point cloud model [29]. The distribution and quantity of ground control points (GCPs) can also impact the accuracy of point cloud models [30]. In addition, an overview of UAV and image-based 3D reconstruction discussed the major factors that influence accuracy and demonstrated the accuracy and limitations of UAV-based topographic surveying [31]. The five influence factors (flight height, average image quality, image overlap, GCP quantity, and camera focal lengths) [32] and seven indices (including proximity to key-point features, distance to GCPs, angle of incidence, camera stand-off distances, number of overlapping images, brightness index, and darkness index) [33] impacting 3D modeling accuracy have been investigated. Moreover, the different software for surveying and 3D reconstruction could also affect the accuracy of point cloud models [9].

The point cloud model of engineering structures is mostly reconstructed with centimeter accuracy using images captured by the UAV, which is used for structural damage inspection [34]. Moreover, the region-scale point cloud model can be reconstructed with centimeter accuracy using image-based 3D reconstruction [33]. The millimeter-scale resolution of the point cloud model is displayed for infrastructure condition assessment using an image-based systematic and adaptive reconstruction technique [35]. Even when compared with the point cloud model acquired by a terrestrial laser scanner, the point cloud model reconstructed by multiview images is sufficiently accurate for structural damage inspection and state assessment [35, 36]. The accuracy of the point cloud model is the foundation of engineering applications such as structural health monitoring, damage inspection, and state assessment.

Furthermore, structural condition inspection and damage diagnosis based on the point cloud model have also been studied [37]. The health monitoring of the structural movement can be realized by comparing the data collected by the UAV over different periods [38]. The semantic segmentation of important structural components in the point cloud model can be accomplished for different types of structures, such as bridges [39], tunnels [40], buildings [41], and towers [42]. Structural damage inspection of structural components, such as beams, columns, and walls, is performed easily after structural semantic segmentation in the point cloud model [43]. Moreover, the structural damage inspection of the accurate point cloud model can provide accurate detection results, which can be used as the research basis for structural state assessment [44, 45]. Therefore, the precision of the point cloud model is critical in the processes of structural health monitoring, semantic segmentation, damage inspection, and state assessment. Thus, a feasible method that can realize accurate point cloud model reconstruction of engineering structures is fundamental and necessary.

This paper presents an accurate point cloud model reconstruction method for earthquake-damaged structures based on images captured by UAVs; the effects of different factors on the precision of the point cloud model are examined. First, the methodologies of image-based 3D point cloud model reconstruction and point cloud model quality evaluation are detailed. Thereafter, two real-world multistory earthquake-damaged building structures, corresponding to moderate damage and near-collapse conditions, are illustrated. The influence rules of the main factors, including the number of GCPs, distribution of GCPs, flight manner of the UAV, and distance from the UAV to the target, on the precision of the point cloud model are presented. Finally, the structural damage inspection and state assessment are presented using an accurate point cloud model. In addition, the inspection results of the image-based point cloud model are quantitatively compared with those of the total station and terrestrial laser scanner point cloud model.

Generally, this paper may be distinguished from the existing studies with the following remarks: (1) the selection and distribution of field GCPs are studied to analyze the accuracy and computational efficiency of UAV-based point cloud models for seismic damaged structures; (2) different UAV flight modes, such as automatic and manual flights and close and far flights, are studied to analyze the accuracy and resolution of UAV-based point cloud models; and (3) the residual deformation measured by three methods, including the total station, image-based point cloud model, and terrestrial laser scanner point cloud model, is compared for performance validation on structural damage inspection of point cloud models. Practically, the proposed method could accelerate the field inspection of seismically damaged structures in a digital and efficient manner with UAV equipment and computer vision techniques.

2. Methodology

The proposed methodology of image-based 3D point cloud model reconstruction involves a workflow with four fundamental steps, as shown in Figure 1. (1) First, GCPs are manually placed around the physical structure according to the circumstances. Traditional surveying instruments, such as total

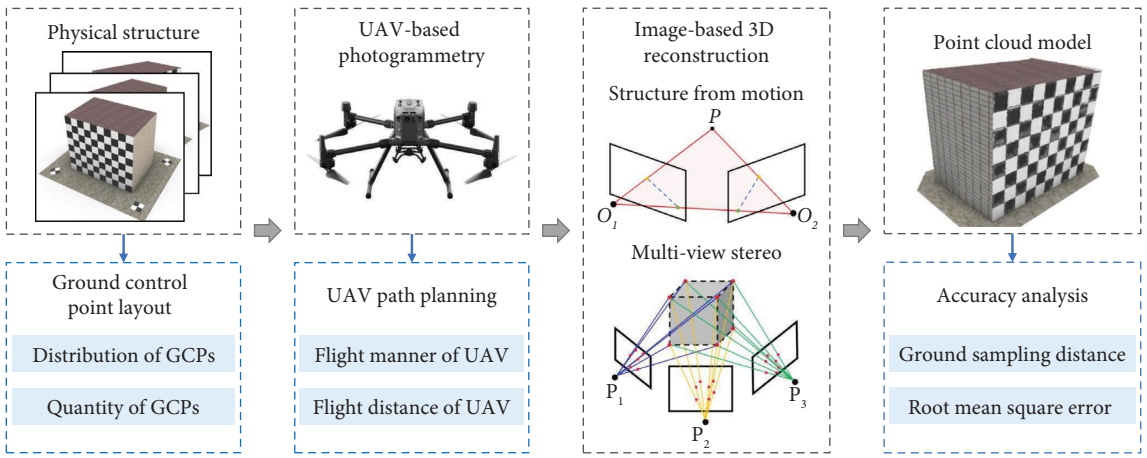

Figure 1: Workflow of image-based 3D point cloud models reconstruction.

stations, are usually used to measure the coordinates of the GCPs for accurate reconstruction. (2) Thereafter, data collection is conducted. Critical image data from different views are captured by photography using UAVs after path planning. To ensure data precision, high-resolution images must be captured. (3) Image-based 3D reconstruction algorithms [46], such as structure from motion (SFM) [31] and multiview stereo (MVS) [33], are adopted to generate a dense point cloud model of the object from multiple images captured by the UAVs. (4) Finally, the main factors affecting the precision of the point cloud model are presented. The resolution and accuracy of the point cloud model are analyzed and shown for later structural inspection and monitoring.

2.1. GCPs Layout. The GCPs are points on the ground with known coordinates. In an aerial mapping survey, the GCPs are points that a surveyor can precisely pinpoint; with a handful of known coordinates, it is possible to accurately map large areas. GCPs play an important role in point cloud modeling and are used to locate the position, constrain the size, and check the accuracy. A point that is evidently distinguished in the surrounding environment can be used as a natural GCP. In addition, artificially designed special point patterns, such as white and black papers, can be employed as artificial GCPs because they easily display high-contrast visual characteristics. The quantity and distribution of GCPs may have significant effects on the accuracy of the point cloud model [30], and the edge distributions of GCPs may obtain a better accuracy of the point cloud model [47]. In addition, it is recommended that GCPs be evenly distributed over the interest area [48]. Figure 2 illustrates the uniform, concentrated, and linear distribution of GCPs. Geometrically uniform distribution means GCPs are uniformly distributed in the whole area of interest, as shown in Figure 2(a), and the majority of the target area is covered by GCPs. Concentrated distribution means GCPs are located in a relatively small region, as shown in Figure 2(b); obviously, a small portion of the target area is covered by GCPs. Linear distribution means GCPs are approximately distributed in the area of interest, as shown in Figure 2(c).

2.2. Data Collection. Camera-enabled UAVs provide a method that can significantly facilitate inspection and collect image data from inaccessible regions. UAV path planning allows accurate acquisition of high-quality image data groups for point cloud modeling. Common UAV flight paths include the scan and surround paths (as shown in Figure 3), which are available for regional flight mapping and building flight mapping, respectively. The scan flight paths (as shown in Figure 3(a)) of UAVs collect the visual information of the region from one direction and are suitable for regional flight mapping. The surrounding flight paths (as shown in Figure 3(b)) of UAVs collect the visual information of the target from all directions and are suitable for building flight mapping. Moreover, it is necessary to perform supplementary photography outside the UAV flight paths to ensure the completeness of the data. Adjacent images require a sufficient overlap area to ensure that a reliable connection can be established between the images in the point cloud reconstruction. The accuracy of point cloud models would be improved when increasing the image overlap [32]. Appropriate high values for the forward and side-overlap parameters can satisfactorily improve the accuracy of the results, such as about 80% overlap [49]. Furthermore, the manner of flight of the UAV and the distance from the UAV to the target may affect the accuracy of the point cloud model.

2.3. Point Cloud Reconstruction. SfM is a photogrammetric range-imaging technique for estimating three-dimensional structures from image sequences with a sufficiently coupled area. SfM photogrammetry with MVS can provide hyperscale point cloud models using image sequences acquired from UAV cameras and a network of GCPs. The complete reconstruction of point cloud models is accomplished by performing an entire SfM-MVS workflow, which employs multiple algorithms based on 3D computer vision and photogrammetry techniques. Different algorithms are used for each step of the SfM-MVS method. The typical SfM-MVS workflow implemented by most software packages includes the following sequential steps [50]: feature detection,

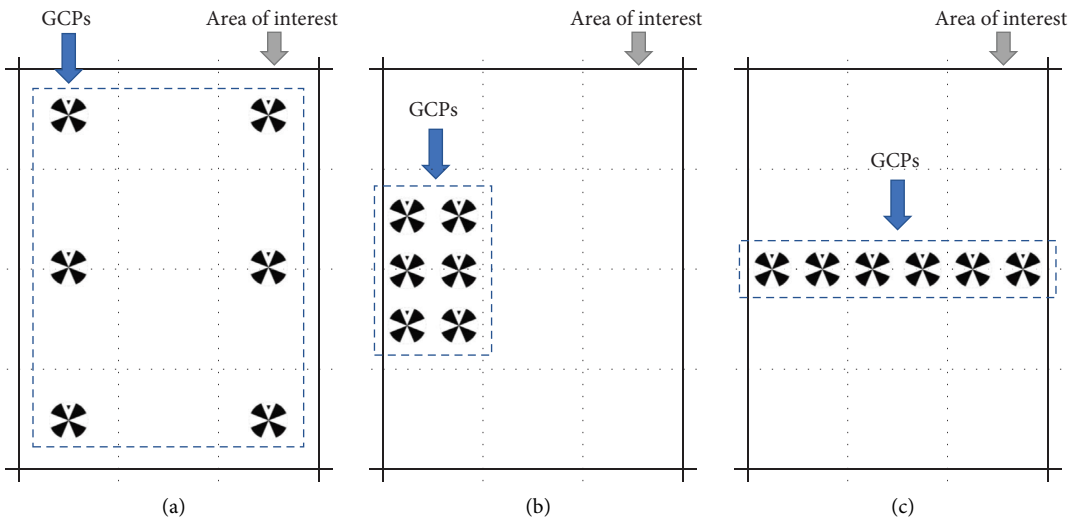

Figure 2: Different distributions of GCPs in the field experiment. (a) Uniform distribution of GCPs. (b) Concentrated distribution of GCPs. (c) Linear distribution of GCPs.

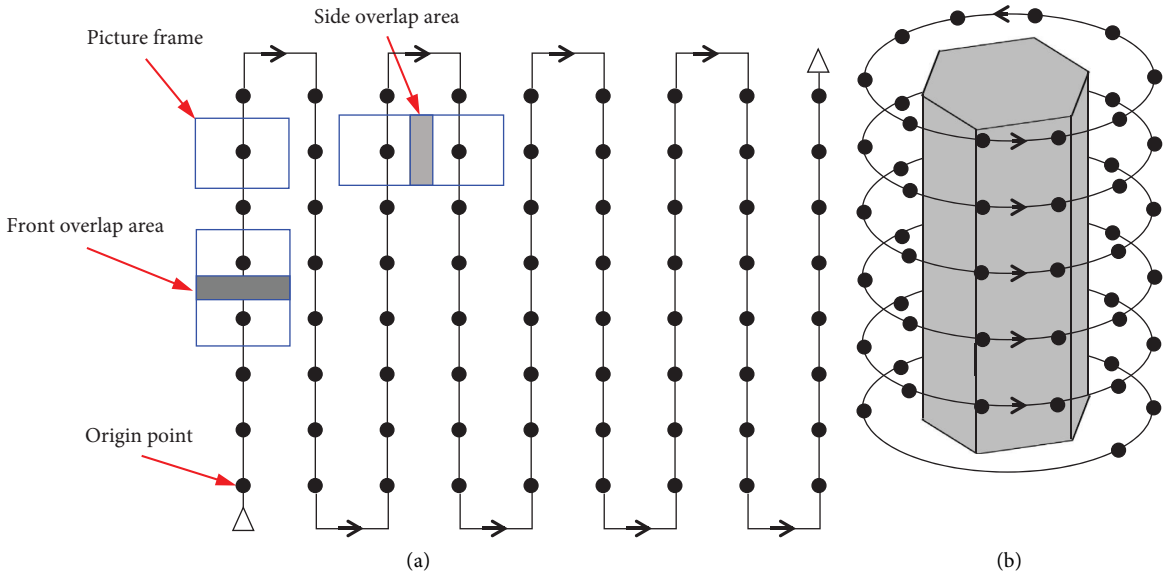

Figure 3: Common UAV flight paths. (a) Scan path. (b) Surround path.

identification of correspondences, identifying geometrically consistent matches and filtering key-point correspondences, structure from motion, scale, and georeferencing, optimization of camera alignment using known GCPs, and point cloud densification.

The computational cost of the SfM-MVS workflow varies depending on various factors such as the number of input images, image resolution, and matching algorithm used. Generally, the computational cost of SfM-MVS can be divided into two main parts: the SfM stage and the MVS stage. (1) The SfM stage involves estimating the camera poses and sparse 3D point clouds from a set of input images. The computational cost of this stage is primarily dependent on the number of images and the complexity of the scene. For example, if the scene has a lot of texture and features, then the number of extracted features and the number of matches will be high, which will increase the computational cost. On the other hand, if the scene is relatively simple and has fewer features, the computational cost will be lower. (2) The MVS stage involves dense reconstruction of the scene from the sparse 3D point cloud obtained from the SfM stage. This stage involves computing the depth for each pixel in the images and fusing them to create a dense 3D model. The computational cost of the MVS stage is primarily dependent on the number of pixels in the images and the resolution of the output point cloud.

In addition, the number of GCPs used in SfM-MVS workflows can impact the computational cost in several ways: (1) Adding GCPs can increase the overall number of tie points, which may increase the computational cost of feature extraction and matching algorithms. (2) GCPs can be used to scale the model and improve its accuracy, which may require

additional computation time during bundle adjustment and dense reconstruction steps. (3) The number and distribution of GCPs can also affect the computation cost of the SfM-MVS workflow. Using a larger number of well-distributed GCPs can lead to faster convergence times during bundle adjustment, whereas using a smaller number of poorly distributed GCPs may result in longer computation times.

The number of GCPs used in SfM-MVS workflows has a significant impact on the accuracy of point cloud models. In general, the more GCPs that are used, the more accurate the reconstruction of the point cloud model will be. This is because more GCPs provide more information for the software to use in calculating the transformation between the point cloud models and the real world. However, it is important to note that there is a point of diminishing returns with adding more GCPs. Beyond a certain number, the additional GCPs may not significantly improve the accuracy of the point cloud model. Additionally, the accuracy of the GCPs themselves also plays a role in the overall accuracy of the point cloud model.

This technique is not limited by a temporal frequency and can provide point cloud data comparable in density and accuracy to those generated by terrestrial and airborne laser scanning at a fraction of the cost. Recently, several existing commercial software packages, such as Pix4Dmapper, Agisoft Metashape, and ContextCapture, have realized image-based point cloud reconstruction. Several existing literature [51, 52] have studied the performance of different software in terms of accuracy and speed of point cloud models reconstruction and show that different software has its own advantages. Agisoft Metashape and Pix4Dmapper were found to have better performance than ContextCapture, which had a worse accuracy of point cloud models reconstruction than other software due to limitations in the performance of the image matching algorithm [51, 52]. In addition, Pix4Dmapper was found to have similar performance [51, 53–55] with Agisoft Metashape in accuracy of point cloud models reconstruction and have better density [51] than Agisoft Metashape.

2.4. Model Quality Evaluation. The average Ground Sampling Distance (GSD) [48] and Root Mean Square Error (RMSE) [56], common indicators for the quality evaluation of point cloud models, indicate the resolution and accuracy of the point cloud models, respectively. GSD is a measure of one sampling limitation to spatial resolution, which is the distance between two consecutive pixel centers measured on the ground. The larger the value of GSD, the lower the spatial resolution of the image and the less visible the details. The calculation of GSD is shown in equations (1)–(3):

$$\mathrm{GSD}_h = \frac{H \times S_{\mathrm{height}}}{f \times \mathrm{Img}_{\mathrm{height}}}, \tag{1}$$

$$\mathrm{GSD}_w = \frac{H \times S_{\mathrm{width}}}{f \times \mathrm{Img}_{\mathrm{width}}}, \tag{2}$$

$$\mathrm{GSD} = \max\left(\mathrm{GSD}_h, \mathrm{GSD}_w\right), \tag{3}$$

where f denotes the focal length of the camera. H is the UAV's flight altitude. S_{height} and S_{width} are the height and width of the camera sensor, respectively. $\mathrm{Img}_{\mathrm{height}}$ and $\mathrm{Img}_{\mathrm{width}}$ are the image height and width in pixels, respectively.

The RMSE is the square root of the mean of the square of the error between the coordinates of the GCPs and the corresponding points in the point cloud model. RMSE is commonly applied, and it is considered an excellent general metric for the accuracy of point cloud models. The three dimensions and total RMSE are calculated using equations (4)–(7):

$$\mathrm{RMSE}_X = \sqrt{\frac{1}{n}\sum_{i=1}^{n}\left(X_{\mathrm{p}}(i) - X_{\mathrm{t}}(i)\right)^2}, \tag{4}$$

$$\mathrm{RMSE}_Y = \sqrt{\frac{1}{n}\sum_{i=1}^{n}\left(Y_{\mathrm{p}}(i) - Y_{\mathrm{t}}(i)\right)^2}, \tag{5}$$

$$\mathrm{RMSE}_Z = \sqrt{\frac{1}{n}\sum_{i=1}^{n}\left(Z_{\mathrm{p}}(i) - Z_{\mathrm{t}}(i)\right)^2}, \tag{6}$$

$$\mathrm{RMSE} = \sqrt{\mathrm{RMSE}_X{}^2 + \mathrm{RMSE}_Y{}^2 + \mathrm{RMSE}_Z{}^2}, \tag{7}$$

where X_{p}, Y_{p}, and Z_{p} represent the three-dimensional coordinates in the point cloud model; X_{t}, Y_{t}, and Z_{t} represent the three-dimensional coordinates measured by surveying instruments; and n is the number of GCPs.

3. Experimental Study

In this study, two earthquake-damaged buildings, which experienced the M_S 8.0 Wenchuan earthquake on May 12, 2008, were selected to study the image-based 3D reconstruction technology. Both structures were located in Beichuan County, Sichuan Province. In the first example, a four-story masonry structure with moderate damage, is used for investigating the effect of UAV flight manner, distance from UAV to target, and quantity of GCPs on the accuracy of the point cloud model. The second example is a three-story reinforced concrete frame structure with a near-collapse status for examining the effect of the distribution of GCPs on the accuracy of the point cloud model.

3.1. Four-Story Masonry Building. Because of the open environment around the four-story masonry building structure, the surrounding flight path of UAVs is suitable for the collection of images. Considering the duration of fieldwork and accuracy of point cloud models [30], 13 GCPs are selected for controlling the accuracy of point cloud models and researching the quantity of GCPs. The actual scene of the four-story masonry building with 13 GCPs layouts is shown in Figures 4(a) and 4(b) from two directions: the east and west sides. The selected 13 GCPs are evenly distributed on

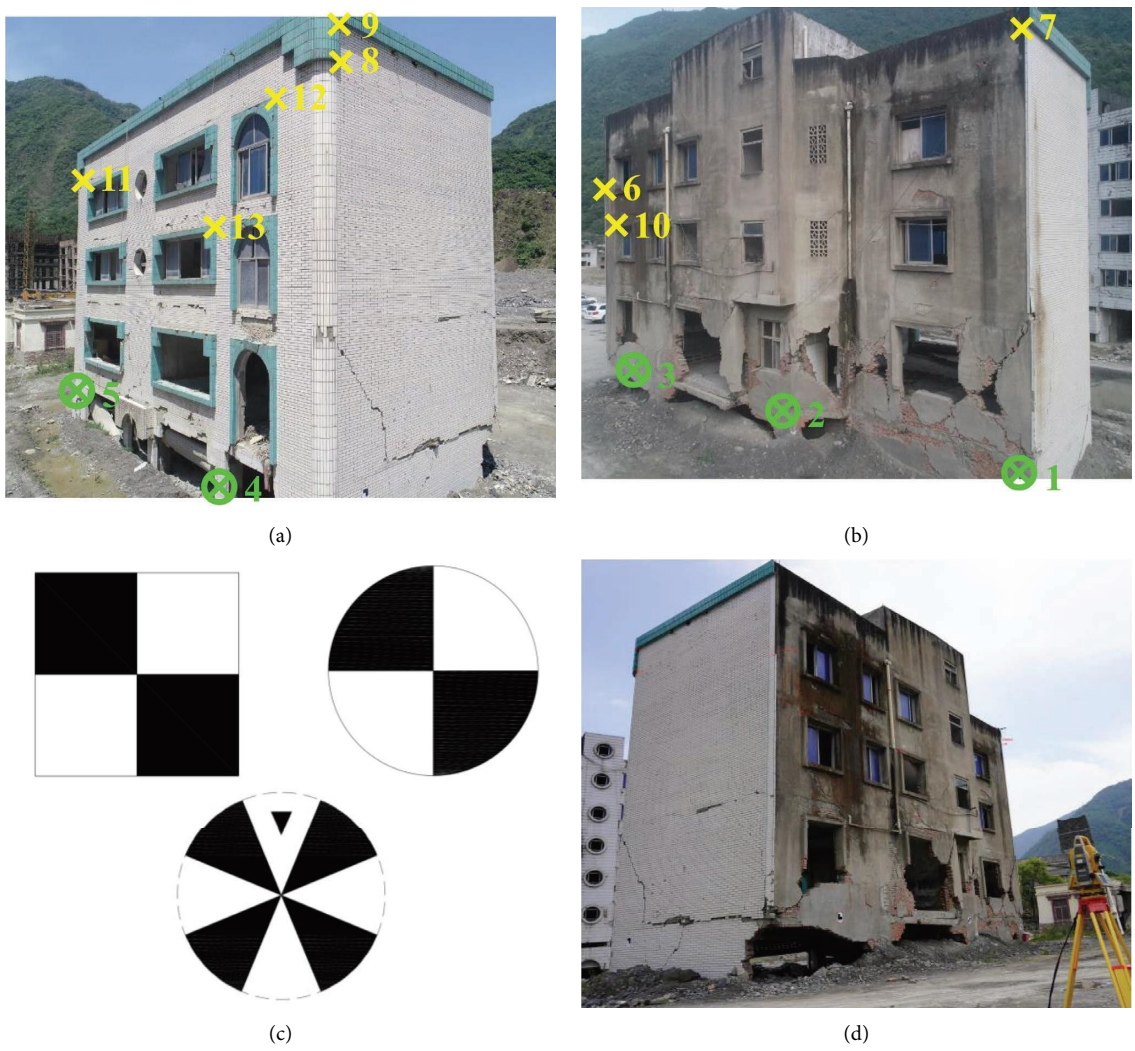

FIGURE 4: Layout and field measurement of GCPs in the four-story masonry building. (a) GCPs layout: east side. (b) GCPs layout: west side. (c) Artificial GCPs. (d) Field survey.

the structure surface, in which GCPs Nos. 1–5 laid near the ground are artificial with black and white patterns identified in Figure 4(c). In addition, GCPs Nos. 6–13 on the building surface, such as points in corners and edges, are natural and clearly distinguished in the surrounding environment. Since the damaged building is inaccessible, the five artificial GCPs covering all directions of the structure are uniformly laid near the ground on the building surface. It is difficult to identify multiple corners with distinct colors as natural GCPs on the dark west side of the building. Thus, three natural GCPs are laid on the west side of the target building, and five natural GCPs are utilized on the east side of the building. The TOPCON GPT-7502 total station was used as a surveying instrument to measure the coordinates of the GCPs, as shown in Figure 4(d). The coordinates of the GCPs measured by the total station were adjusted to a range of 10~30 m for better calculations, as shown in Table 1.

The DJI Phantom 4 Pro drone was used for field photogrammetry with camera angles of 0° and -30° in different flight modes to ensure that 2000 images with approximately 75% front and side overlap area were captured with an image resolution of 5472×3648 pixels, as shown in Figure 5(a). Four UAV flight modes were selected because of the flight manner and surrounding radius of the UAV, including automatic close surround path, automatic far surround path, manual close surround path, and manual far surround path, as shown in Figures 5(b) and 5(c). The images taken by the automatic surround path were uniformly distributed in space and had a consistent overlap area ratio. The images captured by the manual surround path were relatively scattered in space and had diverse overlap area ratios. Subsequently, the point cloud models were reconstructed by image-based 3D reconstruction based on images from different UAV flight modes: a manual surround path with surround radii of 15 m and 20 m, an automatic surround path with surround radii of 15 m and 20 m, and a combination of manual and automatic surround paths with surround radii of 15 m and 20 m, as shown in Table 2. Figure 5(d) illustrates the point cloud model from four directions: front, back, and two side views. The point cloud

Table 1: Coordinates of the GCPs measured by the total stations in the four-story masonry building.

GCPs	Coordinates (m)		
	X	*Y*	*Z*
1	19.2387	10.3590	10.5266
2	15.2061	16.8940	10.8716
3	11.2177	24.7296	11.0074
4	19.0987	25.8111	10.0000
5	24.4490	13.1980	10.6207
6	10.0000	26.9793	18.9569
7	19.0484	10.0000	21.9171
8	16.6691	29.7544	21.0896
9	16.6197	29.8530	22.0654
10	10.4809	26.0054	17.3211
11	24.1948	12.9820	21.0853
12	17.7426	28.2454	20.6279
13	19.0189	25.5135	17.6225

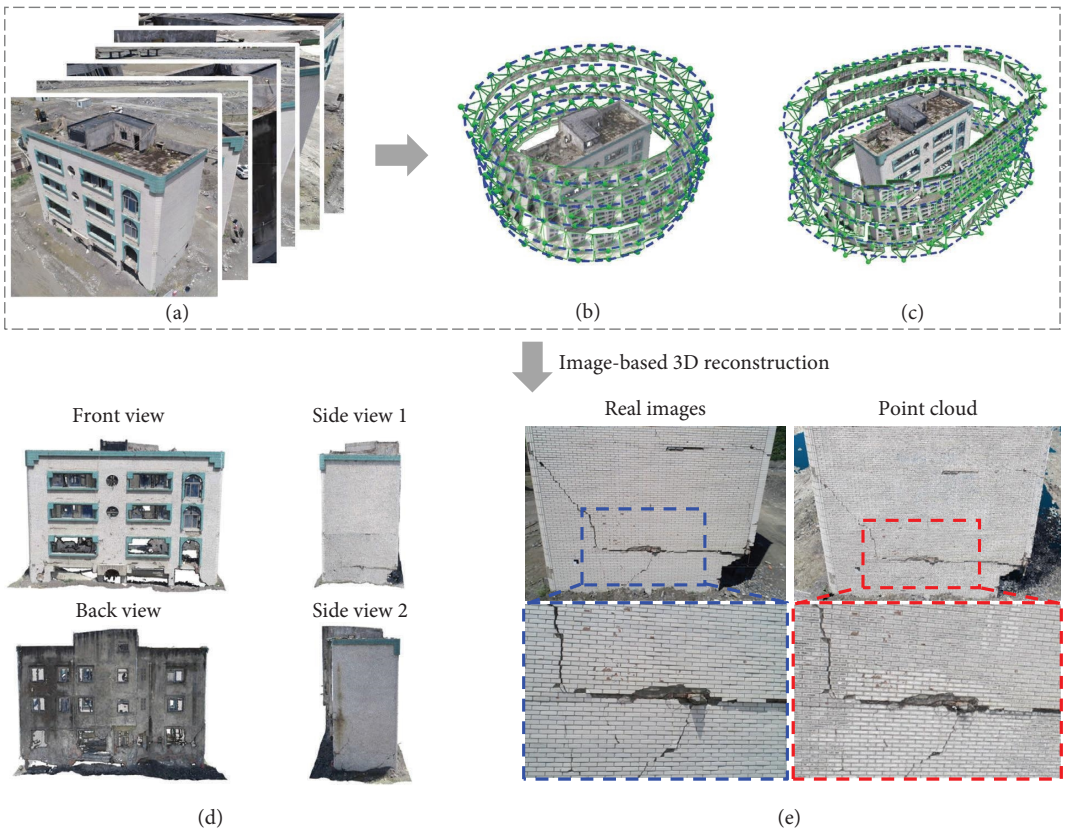

Figure 5: Point cloud model reconstruction of the four-story masonry building. (a) Overview of physical structure. (b) Automatic surround path. (c) Manual surround path. (d) Point cloud model. (e) Local comparison.

model was reconstructed based on images taken by an automatic close surround path. The real-life images and processed point cloud models were further compared with two illustrative damaged regions, as shown in Figure 5(e). The point cloud model can favorably digitalize the original appearance of the physical object, and most of the appearance details can be restored. However, slight deviations may be observed in the color and lighting.

Different software was compared for selecting the software that is most suitable for reconstruction of point cloud models. The computer with the main specifications (CPU: Intel (R) Core (TM) i7-12700 CPU; RAM: 64 GB; GPU: NVIDIA GeForce RTX3060) was used for selection of suitable software. The comparison of point cloud models generated by images captured by UAV (automatic close surround path) between three software (ContextCapture,

Table 2: Different UAV flight modes and number of images for 3D reconstruction.

Flight modes	Surround radius (m)	Number of images
Manual surround path	15	612
	20	439
Automatic surround path	15	503
	20	194
Manual + automatic surround path	15	1115
	20	633

Agisoft Metashape, and Pix4Dmapper) is shown in Table 3, which also shows the version and website of the three software. Figure 6 illustrates the comparison of computational time and model quality between different software. ContextCapture was found to have worse accuracy and speed of point cloud model reconstruction than other software, but more dense point clouds with 546,951,496 points in the model was generated by ContextCapture. The faster speed and better resolution of the point cloud model reconstruction were found in Agisoft Metashape, but more sparse point clouds with 10,713,043 points in the model were generated. Pix4Dmapper was found to have better accuracy of point cloud models reconstruction than other software. Additionally, the moderate speed and density of point cloud modeling were found in Pix4Dmapper. Therefore, Pix4Dmapper, with its balanced performance between efficiency and accuracy, was selected to establish the point cloud model using field-captured image sequences for the current research.

Subsequently, several point cloud models were reconstructed to investigate the influence of the different flight modes on the accuracy of the point cloud model. The different flight modes include a manual surround path with surround radii of 15 m and 20 m, an automatic surround path with surround radii of 15 m and 20 m, and a combination of manual and automatic surround paths with surround radii of 15 m and 20 m, as shown in Table 2. The GSD and RMSE of the point cloud model under any flight mode were less than 20 mm, some of which even reached the millimeter level. Figure 7 shows the effects of the flight manner and surround radius of the UAV on the GSD and RMSE. Noticeably, the GSD of the manual surround path is smaller than that of the automatic surround path, and the GSD of the close surround path is smaller than that of the far surround path, as shown in Figure 7(a). This ensures that the spatial resolution of the reconstructed point cloud model is higher, indicating that the precision of the point cloud model is better. Furthermore, the RMSE of the automatic surround path is smaller than that of the manual surround path owing to the more consistent overlap area ratio of the images, as shown in Figure 7(b), where the flight surround radius has no effect on the RMSE. The point cloud model based on image combinations captured by automatic and manual surround paths does not have better resolution and accuracy owing to the confused overlap area ratio of the images.

Subsequently, because the selected GCPs are evenly distributed on the structure surface, a series of point cloud models are reconstructed using a variable number of GCPs to study the effect of the number of GCPs on the accuracy of the point cloud model. The importance of the GCP is presented in Figures 8(a) and 8(b), which show a comparison between the point cloud model with and without GCPs. Significant differences in the point cloud model size can be identified, such as the distances from GCP 4 and GCP 11 to GCP 5 in the two point cloud models being different by more than 1 m. The significant difference in the point cloud model size indicates that GCPs are indispensable in image-based point cloud reconstruction owing to the size controls. The four randomly selected work groups on the additive order of the variable number of GCPs are shown in Table 4, which is used for the reconstruction of a series of point cloud models. The RMSE of the point cloud models in the four groups revealed the effect of the number of GCPs on the accuracy of the point cloud model, as shown in Figure 8(c). The 13 GCPs yielded the smallest RMSE of 10.084 mm, indicating the highest accuracy of the point cloud model, whereas the least three GCPs produced the largest RMSE of 25.995 mm, indicating the lowest accuracy of the point cloud model. Evidently, the larger the number of GCPs, the smaller the RMSE of the point cloud model. The RMSE is limited by the accuracy of the GCPs and image quality; there is insignificant change for a number of GCPs exceeding seven.

Additionally, the impact of the GCPs quantity on computational cost was studied. The computer with the main specifications (CPU: Intel (R) Core (TM) i7-12700 CPU; RAM: 64 GB; GPU: NVIDIA GeForce RTX3060) was used for reconstruction of point cloud models. Group I in Table 4 was selected for studying the impact of the GCPs quantity on computational cost. The computational time for each reconstruction is recorded, as shown in Figure 9. A small amount of GCPs does not significantly affect the computational cost. However, a large number of GCPs significantly reduce computational time, as shown in Figure 9(a). The significant correlation between the accuracy of the point cloud model and computational time is shown in Figure 9(b). The larger quantity of GCPs leads to better accuracy of point cloud models and faster efficiency of model reconstruction.

3.2. Three-Story Frame Structure. There are many trees and buildings around the seismically damaged three-story concrete frame structure; therefore, the scan flight path of the UAVs is selected to collect image data. The visible and different inclination conditions were observed on the second floor of the three-story frame structure, providing a unique opportunity for studying point cloud model-based structural damage detection. Therefore, two natural GCPs

Table 3: Comparison of three software and point cloud models reconstructed.

Software	Computational time (min)	Points	Version	Website
Pix4Dmapper	52.33	26, 314, 604	4.7.5	https://www.pix4d.com
Metashape	20.97	10, 713, 043	2.0.1	https://www.agisoft.com
ContextCapture	132.77	546, 951, 496	10.20.0	https://www.bentley.com

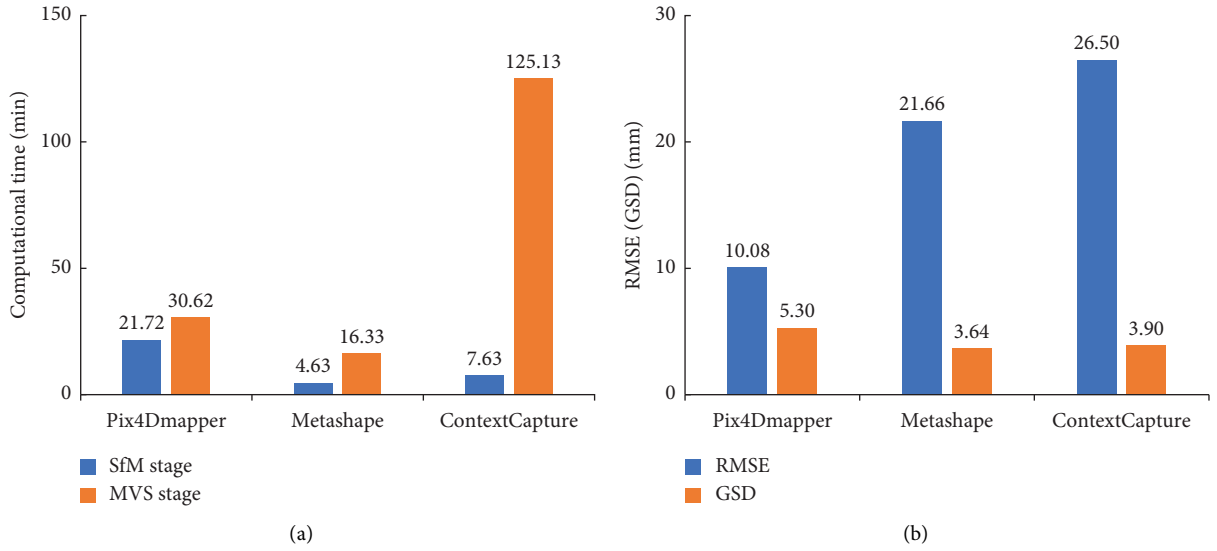

Figure 6: Comparison of performance between different software. (a) Comparison of computational time between different software. (b) Comparison of model quality between different software.

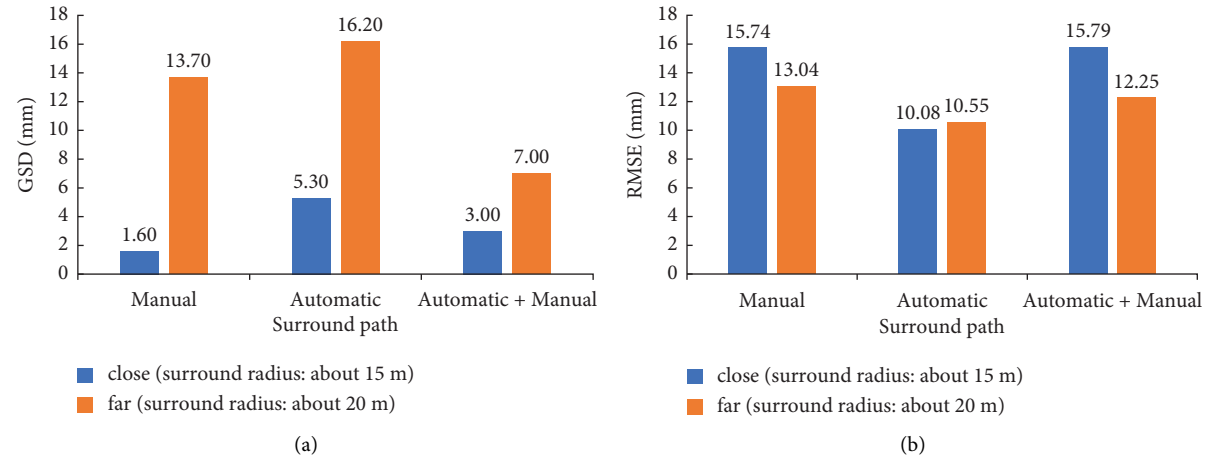

Figure 7: Effect of flight modes on the GSD and RMSE. (a) Effect of flight modes on the GSD. (b) Effect of flight modes on the RMSE.

are laid on each column of the second floor to control the accuracy of point cloud models. In addition, in order to study the distribution of GCPs, three natural GCPs are uniformly laid on the distinguished corners of the upper part of the frame structure, and four artificial GCPs are laid on the accessible part of the frame structure. The seismically damaged three-story concrete frame structure with multiple GCPs, as shown in Figure 10, was reconstructed based on images for examining the effect of the distribution of GCPs on the point cloud model. Numerous GCPs were regularly distributed on the structure surface, and the coordinates of the GCPs measured by the TOPCON GPT-7502 total station were adjusted to a range of 10~40 m for improved calculation, as shown in Table 5. GCPs 1–23 located on the building surface were natural and clearly distinguished in the surrounding environment. In addition, GCPs No. 24–27 laid near the ground were artificial with black and white patterns. Furthermore, 348 images with approximately 75% front and side overlap areas were captured with an image resolution of 5472×3648 pixels using the DJI Phantom 4 Prodrone in the scan path with camera angles of 0° and −30°.

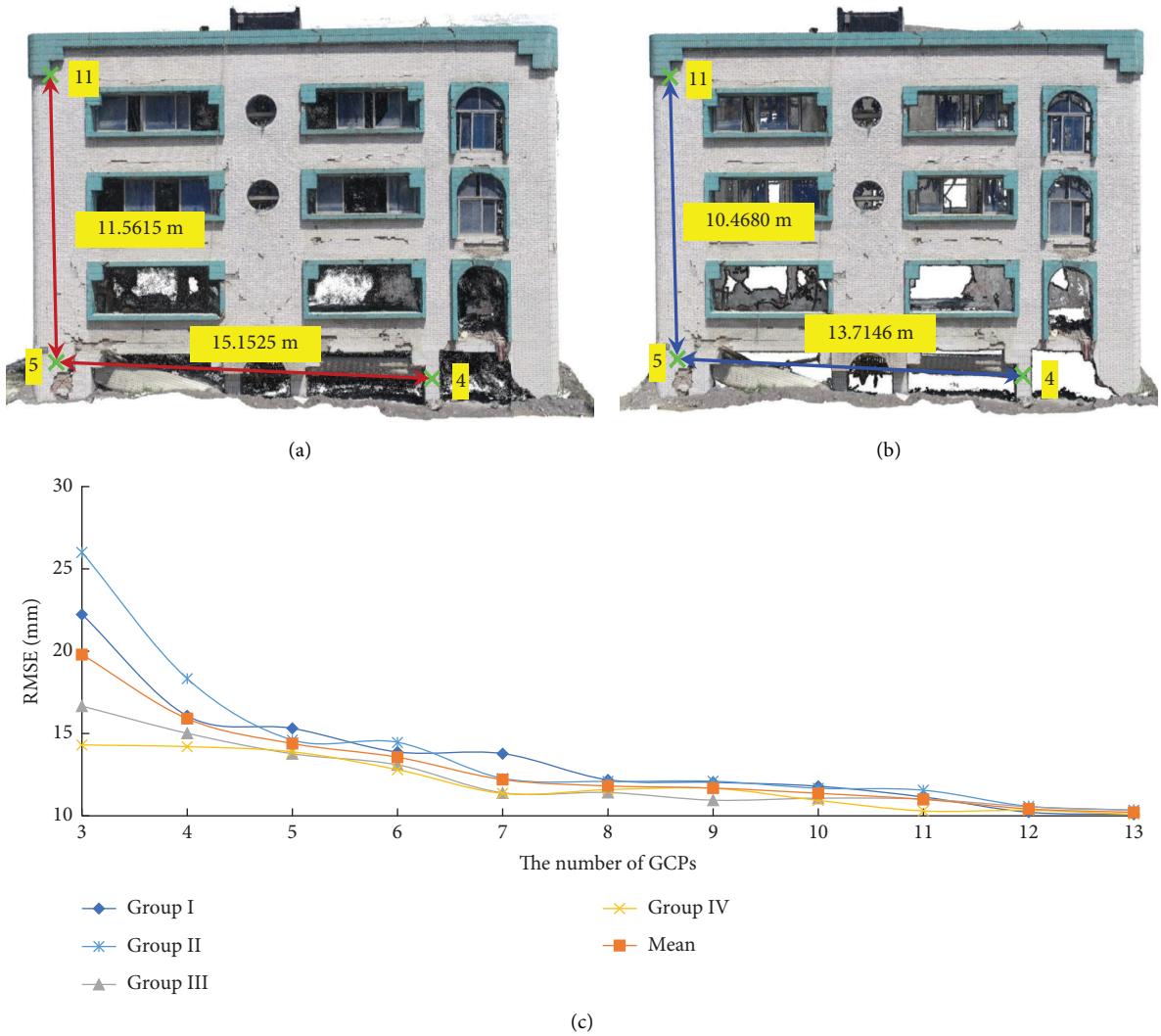

Figure 8: Effect of GCPs on the accuracy of the point cloud model. (a) Point cloud model without GCPs. (b) Point cloud model with GCPs. (c) Effect of the number of GCPs on the RMSE.

Table 4: Four work groups about additive order of the variable number of GCPs.

Work groups	Selected 3 GCPs	Additive GCPs order
Group I	1, 2, 3	4, 5, 6, 7, 8, 9, 10, 11, 12, 13
Group II	11, 12, 13	10, 9, 8, 7, 6, 5, 4, 3, 2, 1
Group III	3, 7, 11	1, 5, 9, 13, 12, 10, 8, 6, 4, 2
Group IV	6, 7, 9	11, 13, 5, 2, 8, 4, 10, 12, 1, 3

The point cloud model of the seismically damaged three-story frame structure was reconstructed using the SfM and MVS techniques based on 27 GCPs and 348 images. The GSD and RMSE of the point cloud model were 2.4 and 6.78 mm, respectively. Figure 11(a) illustrates the point cloud model from three directions (front view and two side views) with complete structural members, such as beams, columns, and walls. The local damage in the point cloud model is clear for structural inspection, although non-structural members, such as glasses, are not completely reconstructed. The real-life images and processed point cloud models were further compared with two illustrative regions, as shown in Figure 11(b). It can be observed that the point cloud model can digitalize the original appearance with slight deviations regarding color and lighting.

Because numerous GCPs are regularly distributed on the structure surface, the different spatial distributions of the GCPs can be used for point cloud reconstruction, as shown in Table 6, with five work groups, including four 4GCPs groups and one 27GCPs group. The GCPs in work groups 4GCPs-I and 4GCPs-II were widely distributed in the model, and the GCPs in work groups 4GCPs-III and 4GCPs-IV were locally distributed in the model. The errors of the GCPs in each spatial distribution are shown in Figure 12. Noticeably, the error of the GCPs is affected by their different spatial distributions. For the selected GCPs (marked with black squares) for reconstruction and the GCPs around them, the error is equal to or smaller than the model error of 27 GCPs for reconstruction. In contrast, there are larger errors in the GCPs that are further from the selected GCPs

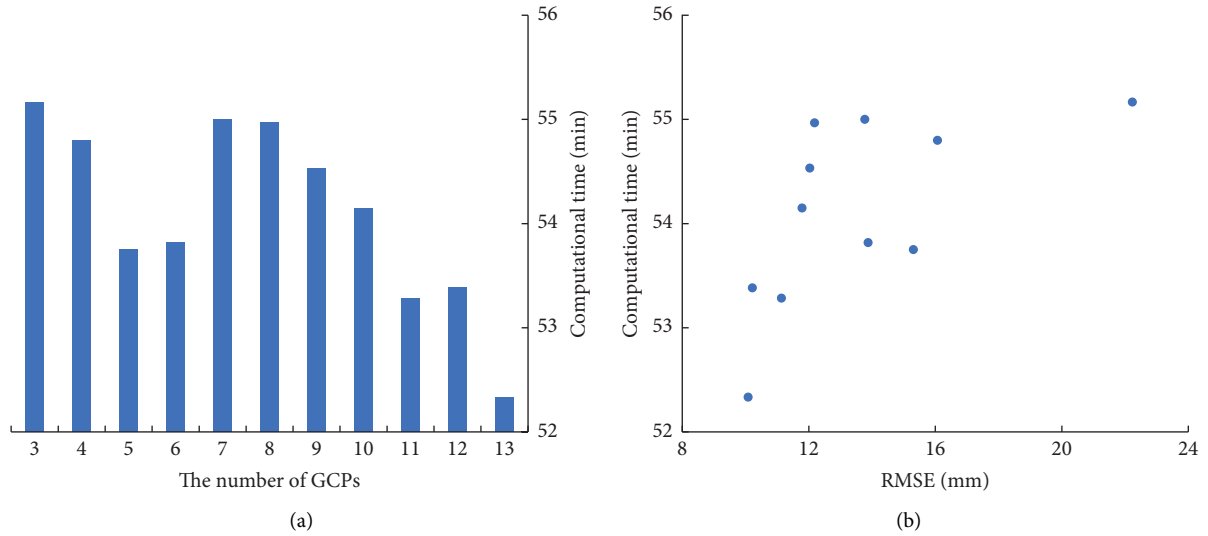

Figure 9: Effect of the GCP quantity on the computational time. (a) Effect of the number of GCPs on computational time. (b) Effect of RMSE on computational time.

Figure 10: Overview of the three-story frame structure and layout of GCPs.

for reconstruction. The error of the point cloud model reconstructed using GCPs widely distributed in the model, such as the work groups 4GCPs-I and 4GCPs-II, is similar to that of the 27 GCPs reconstruction model, as shown in Figures 12(a) and 12(b). The error of the model that is reconstructed using GCPs distributed in the model local area, such as the work groups 4GCPs-III and 4GCPs-IV, is larger than that of the 27 GCPs reconstruction model, as shown in Figures 12(c) and 12(d). In particular, the error of the GCPs further from the local area is larger, such as GCPs 9, 10, 19, 20, 23, and 27 in the 4GCPs-III group and GCPs 21, 22, and 23 in the 4GCPs-IV group.

PCA can be used to interpret the spatial distribution characteristics of GCPs. The products of the eigenvalues of the PCA, shown in Table 6, represent the spatial distribution characteristics, and their effect on the RMSE is shown in Figure 13(a). There are different eigenvalues in the different GCPs distributions, and a larger product of the eigenvalues of the PCA results in a smaller RMSE. For the same number of GCPs, the maximum product of eigenvalues (606.122) in 4GCP-I corresponds to a minimum RMSE of 8.48 mm, and the minimum product of eigenvalues (0.001) in 4GCP-IV corresponds to a maximum RMSE of 32.88 mm. Moreover, the error distribution of the different work groups is shown in Figure 13(b); larger products of eigenvalues of the PCA result in small errors of more quantities, such as 70% error $\leq$5 mm, and large errors of fewer quantities, such as 7% error $\geq$10 mm, in the 27GCPs group. Correspondingly, smaller products of eigenvalues of PCA lead to large errors in more quantities, such as 70% error $\geq$10 mm, and small errors in fewer quantities, such as 22% error $\leq$5 mm, in the 4GCPs-IV group. Therefore, a better spatial distribution with a larger product of eigenvalues of PCA can result in higher accuracy of the point cloud model.

Table 5: Coordinates of the GCPs measured by the total station in the three-story frame structure.

GCPs	Coordinates (m)		
	X	*Y*	*Z*
1	27.3375	38.5120	17.4481
2	25.3773	35.2906	17.7761
3	23.3401	31.9497	17.8342
4	21.3050	28.6382	18.3299
5	19.5552	25.6982	18.4016
6	17.5018	22.1745	18.2681
7	15.3437	18.7225	18.1234
8	13.9724	16.4583	18.1619
9	12.0018	13.2312	18.6124
10	10.0444	10.0000	18.4487
11	28.0751	38.0856	14.7197
12	25.9499	34.9744	15.2006
13	23.8496	31.6710	15.0272
14	21.7602	28.3946	15.0978
15	19.8801	25.5232	15.1341
16	17.4811	21.8047	15.6056
17	15.4405	18.6630	15.6507
18	14.0225	16.4341	15.6922
19	12.0057	13.2393	15.7407
20	10.0000	10.0079	15.7732
21	26.2346	36.9075	23.0972
22	18.2532	23.5400	23.9181
23	11.2902	12.0109	23.5430
24	26.2890	34.5713	10.7282
25	21.2082	28.6444	10.0000
26	17.8271	21.8895	11.4134
27	11.9951	12.9842	11.6362

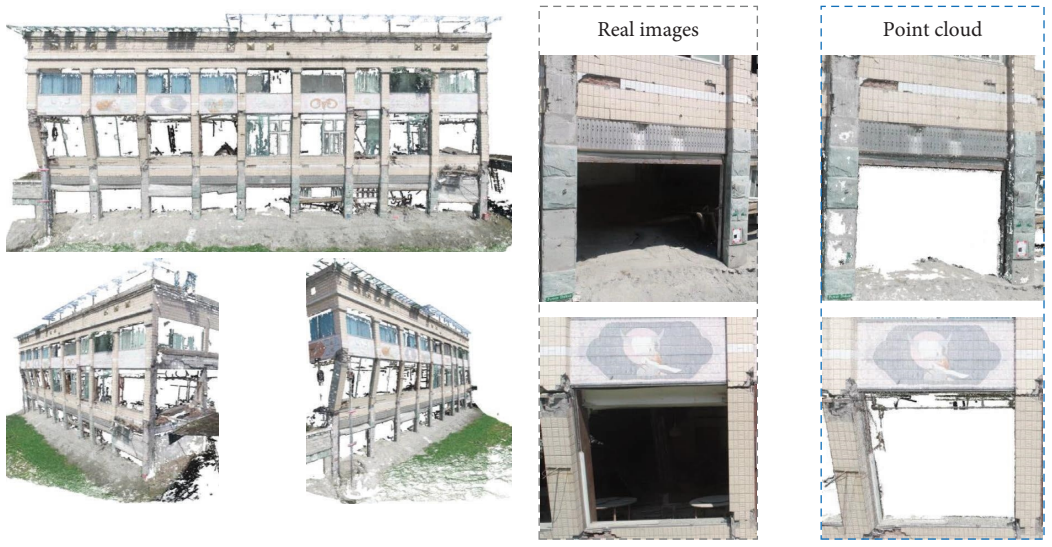

Figure 11: Point cloud model reconstruction of the three-story frame structure. (a) Point cloud model of the frame structure. (b) Local comparison.

Additionally, the impact of the GCPs distribution on computational costs was studied. The computer with the main specifications (CPU: Intel (R) Core (TM) i7-12700 CPU; RAM: 64 GB; GPU: NVIDIA GeForce RTX3060) was used for reconstruction of point cloud models. The computational time for each reconstruction is recorded as shown in Table 6. There is a significant trend between GCPs distribution and computational time, as shown in Figure 14(a).

Table 6: Five work groups and eigenvalues of principal component analysis (PCA).

Work groups	Selected GCPs	Eigenvalues of PCA			Product of eigenvalues	RMSE (mm)	Time (min)
4GCPs-I	21, 23, 24, 27	189.2073	37.0051	0.0866	606.122	8.48	37.38
4GCPs-II	1, 4, 17, 20	19.1566	1.8654	0.0049	0.176	10.54	38.00
4GCPs-III	1, 2, 11, 12	3.6451	1.8478	0.0014	0.009	23.75	38.07
4GCPs-IV	11, 14, 17, 20	156.5007	0.0084	0.0004	0.001	32.88	38.65
27GCPs	All GCPs	763.7671	77.8681	0.3898	23181.417	6.78	38.97

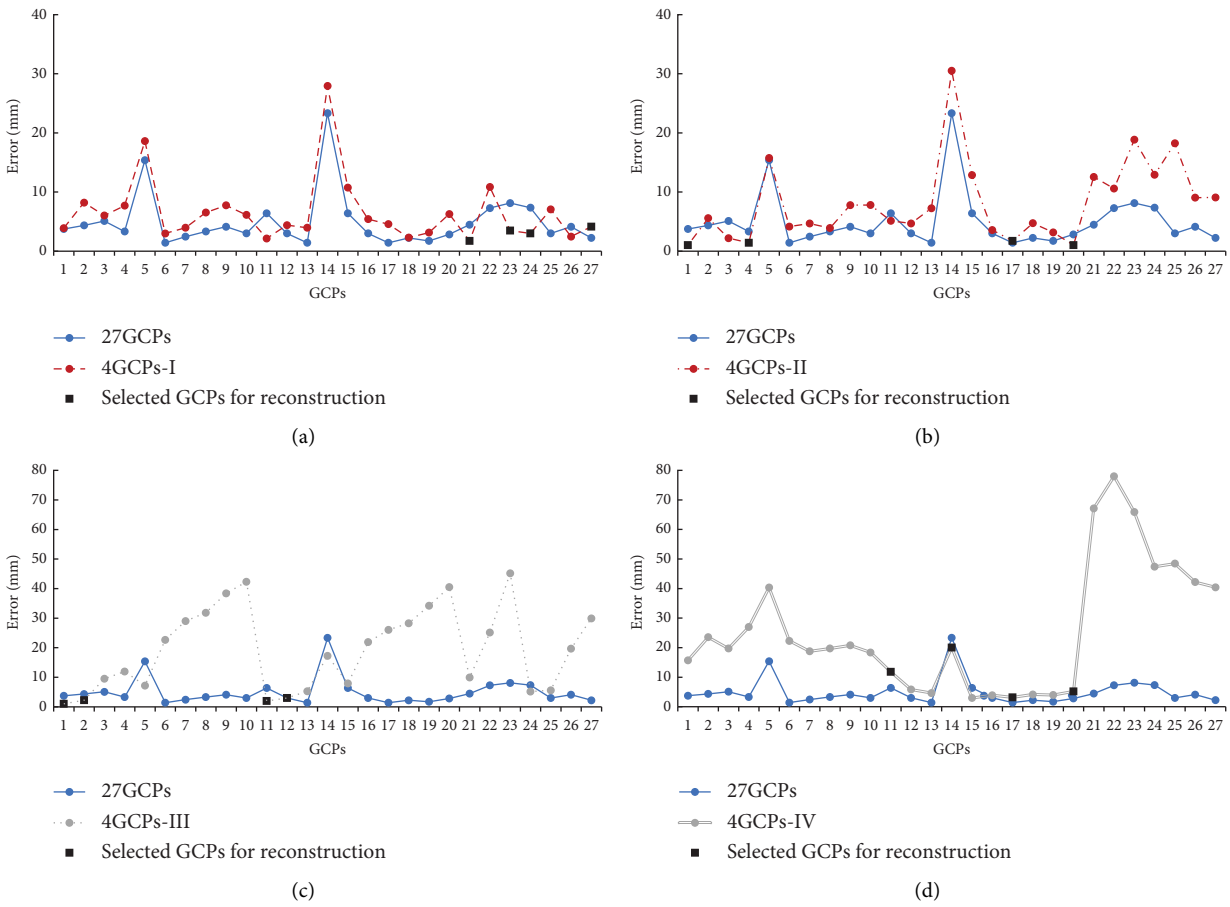

Figure 12: Error of the GCPs in five work groups. (a) 4GCPs-I vs. 27GCPs. (b) 4GCPs-II vs. 27GCPs. (c) 4GCPs-III vs. 27GCPs. (d) 4GCPs-IV vs. 27GCPs.

Figure 14(b) illustrates the significant correlation between the accuracy of the point cloud model and computational time. The wider distribution of GCPs leads to better accuracy and faster efficiency of reconstruction for point cloud models.

An accurate point cloud model can be used for structural damage inspection. A prior study [44] realized the measurement of structural inclination and deformation. Each plane of target columns was segmented by semantic segmentation method [44], as shown in Figure 15. The different colors represent points on different planes in 3D space. Firstly, the point cloud model was downsampled by the Voxel Grid method; points were approximately sampled as their centroid in each voxel. The distance between the nearest two points was approximately the size of the voxel, which was commonly set as 0.01~0.1 m. Then, the plane points (marked with solid dots) and noises (marked with hollow dots) were separated in the point cloud model after random sample consensus (RANSAC) and density-based spatial clustering of applications with noise (DBSCAN) methods execution. The threshold in RANSAC was commonly set at 0.005~0.05 m. Finally, the point cloud model was upsampled by the Voxel Grid method. Currently, the sequential processes of downsampling, segmentation, clustering, and upsampling are presented (Figure 15) by combining the voxel grid, RANSAC, and DBSCAN methods, which are motivated to achieve a satisfactory performance balance between the processing efficiency in computation and the inspection accuracy in engineering. The plane equations of columns were calculated by the regression

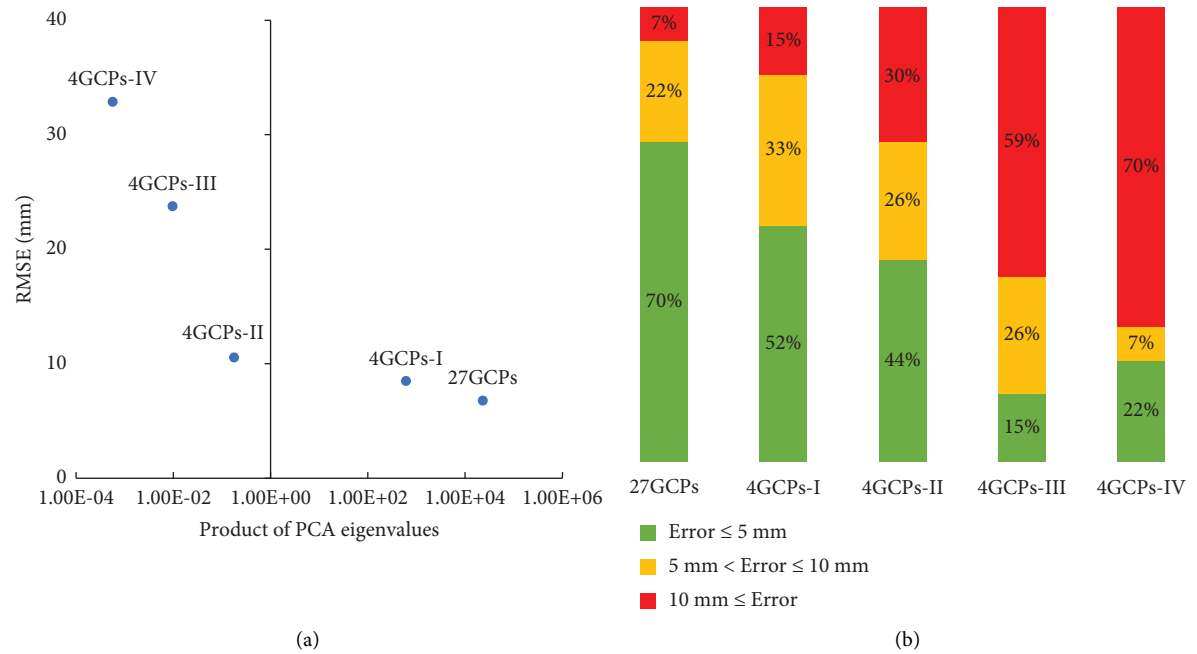

Figure 13: Effect of the GCPs spatial distribution on the accuracy of the point cloud model. (a) Effect of the product of PCA eigenvalues on RMSE. (b) Error distribution among different work groups.

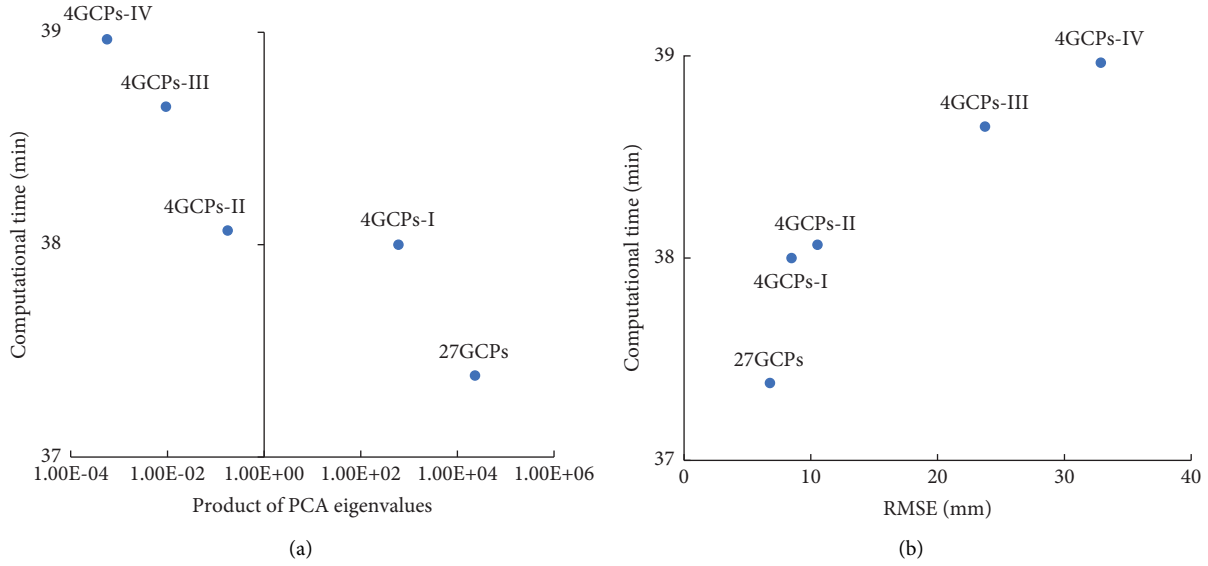

Figure 14: Effect of the GCPs spatial distribution on the computational time. (a) Effect of PCA on computational time. (b) Effect of RMSE on computational time.

method using scatter distribution on the structural surface, and the edges of columns were identified by using plane intersection [44].

Figure 16 shows the details of identification methods for the inclination of columns edges. The normal vector of plane U and V were shown in Figure 16 as $\vec{u}$ and $\vec{v}$, calculated by the plane equations. The edge vector was identified as $\vec{w}$, which was the cross product of $\vec{u}$ and $\vec{v}$. Then, the vector sum of the edges of the column was taken as the inclination vector of the column. The inclination rate and angle of the edge was calculated by decomposing the vector of the edge, which were given as $\vec{w} = (w_x, w_y, w_z)$. The inclination angle θ_w and inclination rate k_w were calculated by equations (8) and (9):

$$\theta_w = \arcsin\left(\frac{|w_z|}{\sqrt{w_x^2 + w_y^2 + w_z^2}}\right), \tag{8}$$

$$k_w = \cot\theta_w. \tag{9}$$

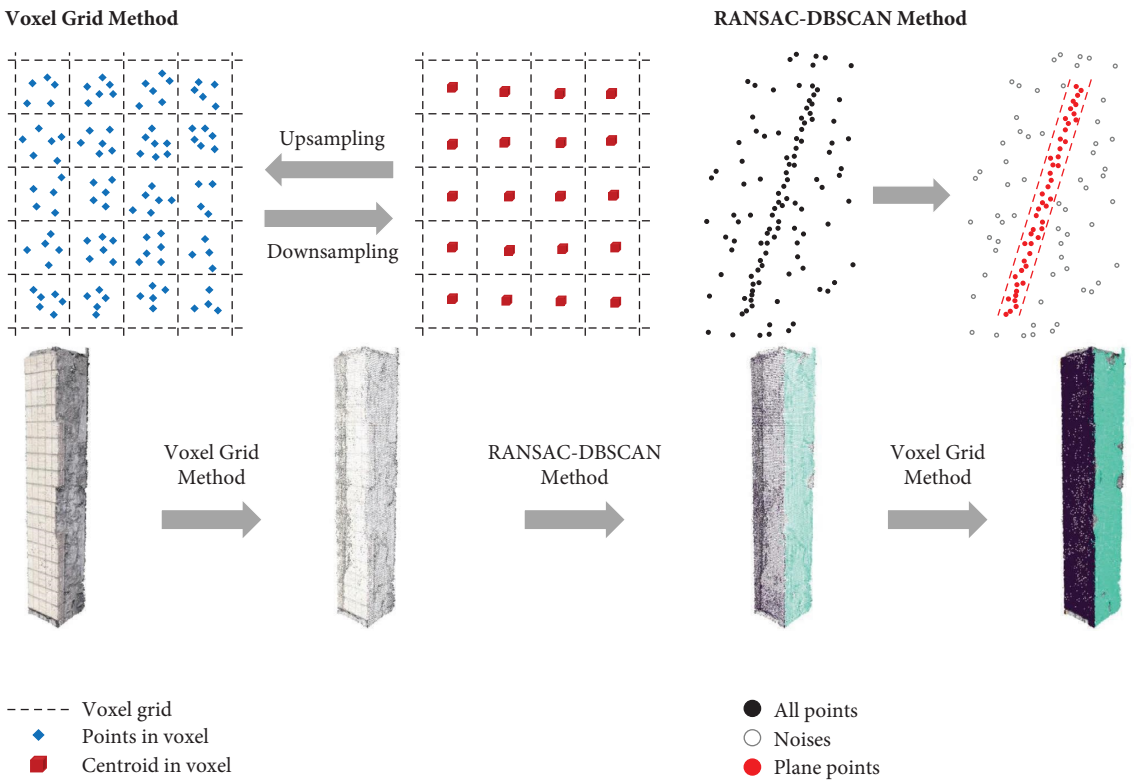

Figure 15: Principles of a structural plane segmentation algorithm based on point cloud models.

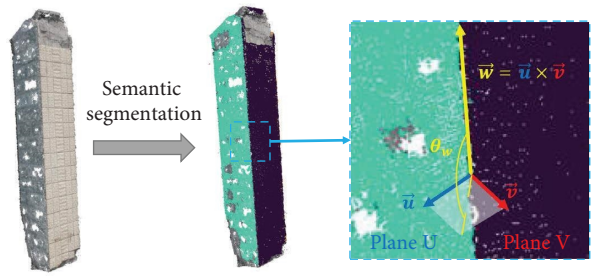

Figure 16: Identification method for edge inclination of columns.

The accuracy and voxel resolution of the point cloud model were the main factors limiting the precision of inclination measurement.

Figure 17(a) shows the segmentation and inclination measurements of the structural columns. The inclination of the 30 columns divided manually was calculated, and the maximum and minimum inclination rates of the columns were 31.359% and 0.316%, respectively. The structure was evaluated as Damage State 4 with the danger of structural collapse from earthquake aftershocks, referring to the code FEMA P-58 [57]. The ten columns on the second floor of the building stayed at obvious and different inclination rates, which ranged from about 0% to about 30%. The column inclination rates on the ground floor and third floor of the frame structure were simpler than those on the second floor. Therefore, the second-floor columns were considered the target inspection object and then measured by the total station. Subsequently, the point cloud model of the seismically damaged three-story concrete frame structure based on image reconstruction and a terrestrial laser scanner was compared to the structural second-floor column inclination measurement. Figure 17(b) shows the comparison of second-floor column inclinations measured by three methods, including the total station measurement, the measurement of the image-based point cloud model, and the measurement of the terrestrial laser scanner point cloud model. The inclination rate of the 10 columns on the second floor could be measured by the three methods from the maximum value of approximately 32% to the minimum value of near 0%, and the inclination rates measured by the three methods were similar. More detailed data and relative errors are presented in Table 7. The inclination measured by the total station was compared with that measured by the two point cloud models, and the relative errors were all within 4%. The average values of relative error of the inclination of the 10 columns were also displayed as 1.543%

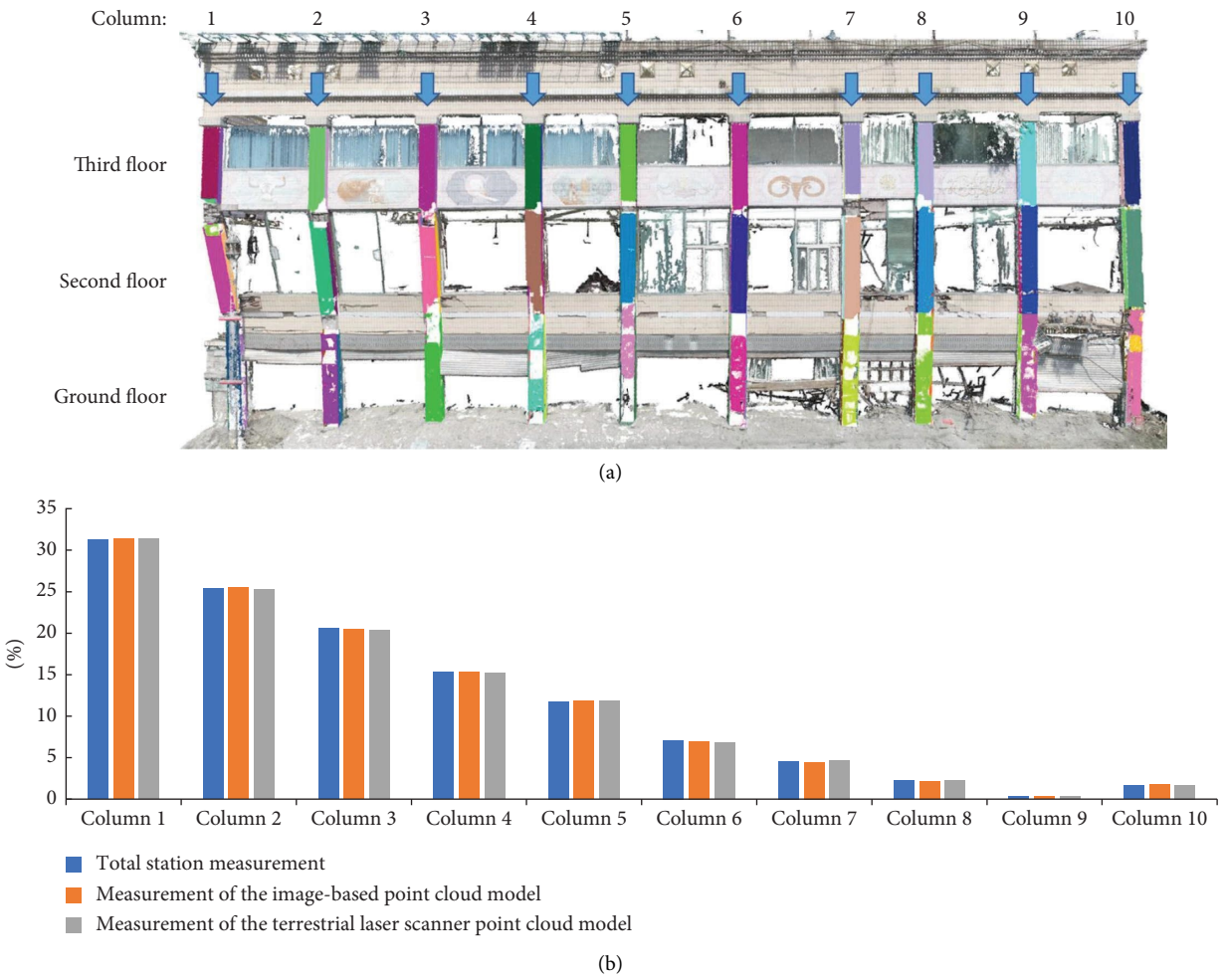

Figure 17: Segmentation and inclination comparison of structural columns. (a) Segmentation and inclination measurement of structural columns. (b) Comparison of second floor inclination measured by three methods.

Table 7: Second-floor column inclination measured by three methods and the relative error.

Target components	TSM (%)	IBM (%)	TLSM (%)	RE of TSM and IBM (%)	RE of TSM and TLSM (%)
Column 1	31.226	31.359	31.377	0.426	0.484
Column 2	25.397	25.486	25.266	0.350	0.516
Column 3	20.573	20.435	20.363	0.671	1.022
Column 4	15.273	15.285	15.226	0.079	0.306
Column 5	11.791	11.861	11.868	0.594	0.653
Column 6	7.095	6.994	6.828	1.424	3.769
Column 7	4.595	4.446	4.688	3.243	2.022
Column 8	2.253	2.168	2.306	3.773	2.330
Column 9	0.313	0.316	0.311	0.958	0.616
Column 10	1.686	1.752	1.721	3.915	2.092
Average value of relative errors:				1.543	1.381

Note. TSM, total station measurement; IBM, measurement of image-based point cloud model; TLSM, measurement of terrestrial laser scanner point cloud model; RE, relative error.

(image-based point cloud model) and 1.381% (terrestrial laser scanner point cloud model). Thus, the accuracy of the image-based point cloud model and the terrestrial laser scanner point cloud model are similar in structural damage inspection.

4. Conclusion

This study investigated the factors influencing the point cloud model reconstruction performance according to two experiments on earthquake-damaged buildings. The performance of common software in point cloud reconstruction was investigated. The main influencing factors, including the flight manner of the UAV, distance from the UAV to the target, number of GCPs, and distribution of GCPs, were studied separately. In addition, the structural damage inspection of accurate point cloud models was presented. The main conclusions are as follows:

(1) Three common software packages, including ContextCapture, Agisoft Metashape, and Pix4Dmapper, were quantitatively compared in terms of point cloud reconstruction performance. ContextCapture was found to have better density, and Metashape was found to have faster speed. Pix4Dmapper outperformed the other packages with a relatively balanced performance, including the best accuracy, moderate speed, and moderate density. Therefore, Pix4Dmapper can be considered a suitable software for point cloud modeling for seismically damaged structures.

(2) The automatic flight manner results in an RMSE of the point cloud model smaller than that of the manual flight manner because of the more consistent overlap area ratio of the images in automatic flight. In addition, a closer distance from the UAV to the target causes a GSD of the point cloud model smaller than that of a farther distance from the UAV to the target. Therefore, the images captured at a close range and in the automatic flight mode of the UAV reconstruct the point cloud model with higher precision and resolution.

(3) The GCPs can control the size and location of the point cloud model to make it the same as the actual target. In addition, more GCPs can reconstruct point cloud models with lower computational costs and better model accuracy. Moreover, a wider distribution of GCPs with a larger product of eigenvalues of PCA can produce point cloud models with lower computational costs, better model accuracy, and fewer large errors. Therefore, more GCPs and a wider distribution of GCPs should be selected for a faster and more accurate reconstruction of point cloud models.

(4) A comparison of 10 column inclinations measured by three methods, including the total station measurement, the measurement of the image-based point cloud model, and the measurement of the terrestrial laser scanner point cloud model, was presented, which showed that the relative errors of inclination rates were all within 4%. Therefore, an accurate point cloud model reconstructed using image-based 3D reconstruction technology is suitable for structural damage inspection and state assessment.

This study provides a theoretical basis for accurate point cloud model reconstruction for earthquake-damaged structures using UAV-based photogrammetry. Thus, after an earthquake, an accurate point cloud model can be reconstructed rapidly for structural damage inspection and state assessment. This provides important support for post-earthquake rescue and resettlement of victims. However, deploying more GCPs with a wider distribution in the field measurement requires more time. Hence, it is important to balance the distribution and quantity of GCPs, which speeds up the reconstruction of accurate point cloud models.

In addition, the accurate point cloud models of building structures are limited in practical engineering applications. The identification of the current structural deformation can be realized by employing a single point cloud model. It may be challenging to realize the measurement of structural incremental deformation with the matching analysis of multiple point cloud models. The structural finite element model may not be fully reconstructed by using structural point cloud models because the inside condition of the structure could not be obtained using UAV-based photogrammetry. In the future, the multisource point cloud model based on the fusion of multiple types of autonomous unmanned equipment (such as unmanned drones and vehicles) is expected to achieve comprehensive structural modeling and diagnosis.

In future studies of the point cloud model precision of image-based 3D reconstruction, an investigation should be conducted on other factors, such as real-time kinematics, and other scenarios, such as regional buildings. Furthermore, the application of accurate point cloud models, such as the extraction of observable physical damage, including surface cracking, wall spalling, and steel component buckling, may also be of interest in the future.

Data Availability

Data used in this study are available upon reasonable request to the corresponding author.

Conflicts of Interest

The authors declare that they have no conflicts of interest.

Acknowledgments

This study was sponsored by the National Natural Science Foundation of China (Grant nos: 51878483 and 52278312), the Shanghai Rising-Star program (Grant no. 20QC1400700), the Shanghai Qi Zhi Institute (Grant no. SYXF0120020109), the Peak Discipline Construction Project of Shanghai (Grant no. 2021-CE-03), and the Shanghai Municipal Science and Technology Major Project (Grant no. 2021SHZDZX0100).

References

[1] Y.-J. Cha, W. Choi, and O. Büyüköztürk, "Deep learning-based crack damage detection using convolutional neural networks," *Computer-Aided Civil and Infrastructure Engineering*, vol. 32, no. 5, pp. 361–378, 2017.

[2] Y.-J. Cha, W. Choi, G. Suh, S. Mahmoudkhani, and O. Büyüköztürk, "Autonomous structural visual inspection using region-based deep learning for detecting multiple damage types," *Computer-Aided Civil and Infrastructure Engineering*, vol. 33, no. 9, pp. 731–747, 2018.

[3] D. Kang, S. S. Benipal, D. L. Gopal, and Y. J. Cha, "Hybrid pixel-level concrete crack segmentation and quantification across complex backgrounds using deep learning," *Automation in Construction*, vol. 118, Article ID 103291, 2020.

[4] J. Lewis, Y.-J. Cha, and J. Kim, "Dual encoder–decoder-based deep polyp segmentation network for colonoscopy images," *Scientific Reports*, vol. 13, no. 1, p. 1183, 2023.

[5] D. H. Kang and Y. J. Cha, "Efficient attention-based deep encoder and decoder for automatic crack segmentation," *Structural Health Monitoring*, vol. 21, no. 5, pp. 2190–2205, 2022.

[6] W. Choi and Y. J. Cha, "SDDNet: real-time crack segmentation," *IEEE Transactions on Industrial Electronics*, vol. 67, no. 9, pp. 8016–8025, 2020.

[7] Y. Han, G. Wu, and D. Feng, "Vision-based displacement measurement using an unmanned aerial vehicle," *Structural Control and Health Monitoring*, vol. 29, no. 10, Article ID e3025, 2022.

[8] H. Zhou, J. Lynch, and D. Zekkos, "Autonomous wireless sensor deployment with unmanned aerial vehicles for structural health monitoring applications," *Structural Control and Health Monitoring*, vol. 29, no. 6, Article ID e2942, 2022.

[9] C. Matteo, R. Umberto, and P. Giovanni, "Structure-from-Motion 3D reconstruction of the historical overpass ponte della Cerra: A comparison between MicMac® open source software and Metashape," *Drones*, vol. 6, no. 9, p. 242, 2022.

[10] B. F. Spencer, V. Hoskere, and Y. Narazaki, "Advances in computer vision-based civil infrastructure inspection and monitoring," *Engineering*, vol. 5, no. 2, pp. 199–222, 2019.

[11] Y. Yan, M. Zhong, and J. Wu, "Towards automated detection and quantification of concrete cracks using integrated images and lidar data from unmanned aerial vehicles," *Structural Control and Health Monitoring*, vol. 28, no. 8, Article ID e2757, 2021.

[12] T. G. Mondal, M. R. Jahanshahi, and R.-T. Wu, "Deep learning-based multi-class damage detection for autonomous post-disaster reconnaissance," *Structural Control and Health Monitoring*, vol. 27, no. 4, Article ID e2507, 2020.

[13] R. Ali, D. Kang, G. Suh, and Y. J. Cha, "Real-time multiple damage mapping using autonomous UAV and deep faster region-based neural networks for GPS-denied structures," *Automation in Construction*, vol. 130, Article ID 103831, 2021.

[14] D. Kang and Y.-J. Cha, "Autonomous UAVs for structural health monitoring using deep learning and an ultrasonic beacon system with geo-tagging," *Computer-Aided Civil and Infrastructure Engineering*, vol. 33, no. 10, pp. 885–902, 2018.

[15] S. Zhao, F. Kang, and J. Li, "Concrete dam damage detection and localisation based on YOLOv5s-HSC and photogrammetric 3D reconstruction," *Automation in Construction*, vol. 143, Article ID 104555, 2022.

[16] C. Biscarini, I. Catapano, N. Cavalagli, G. Ludeno, F. Pepe, and F. Ubertini, "UAV photogrammetry, infrared thermography and GPR for enhancing structural and material degradation evaluation of the Roman masonry bridge of Ponte Lucano in Italy," *NDT and E International*, vol. 115, Article ID 102287, 2020.

[17] A. Ji, X. Xue, Y. Wang, X. Luo, and L. Wang, "Image-based road crack risk-informed assessment using a convolutional neural network and an unmanned aerial vehicle," *Structural Control and Health Monitoring*, vol. 28, no. 7, Article ID e2749, 2021.

[18] Y. Tan, G. Li, R. Cai, J. Ma, and M. Wang, "Mapping and modelling defect data from UAV captured images to BIM for building external wall inspection," *Automation in Construction*, vol. 139, Article ID 104284, 2022.

[19] S. Yoon, B. F. Spencer, and S. Lee, "A novel approach to assess the seismic performance of deteriorated bridge structures by employing UAV-based damage detection," *Structural Control and Health Monitoring*, vol. 29, no. 7, Article ID e2964, 2022.

[20] X. Wang, E. Lo, L. De Vivo, T. C. Hutchinson, and F. Kuester, "Monitoring the earthquake response of full-scale structures using UAV vision-based techniques," *Structural Control and Health Monitoring*, vol. 29, no. 1, Article ID e2862, 2022.

[21] B. K. Oh, S. H. Lee, and H. S. Park, "Damage localization method for building structures based on the interrelation of dynamic displacement measurements using convolutional neural network," *Structural Control and Health Monitoring*, vol. 27, no. 8, Article ID e2578, 2020.

[22] M. P. Limongelli, "SHM for informed management of civil structures and infrastructure," *Journal of Civil Structural Health Monitoring*, vol. 10, no. 5, pp. 739–741, 2020.

[23] Y. Bao, Z. Tang, H. Li, and Y. Zhang, "Computer vision and deep learning–based data anomaly detection method for structural health monitoring," *Structural Health Monitoring*, vol. 18, no. 2, pp. 401–421, 2019.

[24] C. Dorn and Y. Yang, "Automated modal identification by quantification of high-spatial-resolution response measurements," *Mechanical Systems and Signal Processing*, vol. 186, Article ID 109816, 2023.

[25] H. Song and Y. Yang, "Uncertainty quantification in super-resolution guided wave array imaging using a variational Bayesian deep learning approach," *NDT and E International*, vol. 133, Article ID 102753, 2023.

[26] S. Sony, S. Laventure, and A. Sadhu, "A literature review of next-generation smart sensing technology in structural health monitoring," *Structural Control and Health Monitoring*, vol. 26, no. 3, Article ID e2321, 2019.

[27] Y. Yang, X. Liang, B. Wang et al., "Biophysical parameters retrieval of mangrove ecosystem using 3D point cloud descriptions from UAV photographs," *Ecological Informatics*, vol. 72, Article ID 101845, 2022.

[28] Á. Gómez-Gutiérrez, T. Biggs, N. Gudino-Elizondo et al., "Using visibility analysis to improve point density and processing time of SfM-MVS techniques for 3D reconstruction of landforms," *Earth Surface Processes and Landforms*, vol. 45, no. 11, pp. 2524–2539, 2020.

[29] J. Revuelto, J. I. López-Moreno, and E. Alonso-González, "Light and shadow in mapping alpine snowpack with unmanned aerial vehicles in the absence of ground control points," *Water Resources Research*, vol. 57, no. 6, Article ID e2020WR028980, 2021.

[30] E. Ferrer-González, F. Agüera-Vega, F. Carvajal-Ramírez, and P. Martínez-Carricondo, "UAV photogrammetry accuracy assessment for corridor mapping based on the number and distribution of ground control points," *Remote Sensing*, vol. 12, no. 15, p. 2447, 2020.

[31] S. I. Deliry and U. Avdan, "Accuracy of unmanned aerial systems photogrammetry and structure from motion in surveying and mapping: a review," *Journal of the Indian Society of Remote Sensing*, vol. 49, no. 8, pp. 1997–2017, 2021.

[32] Y. Liu, K. Han, and W. Rasdorf, "Assessment and prediction of impact of flight configuration factors on UAS-based photogrammetric survey accuracy," *Remote Sensing*, vol. 14, no. 16, p. 4119, 2022.

[33] F. Javadnejad, R. K. Slocum, D. T. Gillins, M. J. Olsen, and C. E. Parrish, "Dense point cloud quality factor as proxy for accuracy assessment of image-based 3D reconstruction," *Journal of Surveying Engineering*, vol. 147, Article ID 04020021, 2021.

[34] S. Zhao, F. Kang, J. Li, and C. Ma, "Structural health monitoring and inspection of dams based on UAV photogrammetry with image 3D reconstruction," *Automation in Construction*, vol. 130, Article ID 103832, 2021.

[35] K. Ali and D. Lattanzi, "Hierarchical dense structure-from-motion reconstructions for infrastructure condition assessment," *Journal of Computing in Civil Engineering*, vol. 31, no. 1, Article ID 04016047, 2017.

[36] Z. Zhou, J. Gong, and M. Guo, "Image-based 3D reconstruction for posthurricane residential building damage assessment," *Journal of Computing in Civil Engineering*, vol. 30, no. 2, Article ID 04015015, 2016.

[37] L. Wu and F. Casciati, "Local positioning systems versus structural monitoring: a review," *Structural Control and Health Monitoring*, vol. 21, no. 9, pp. 1209–1221, 2014.

[38] P. J. Sousa, A. Cachaço, F. Barros et al., "Structural monitoring of a breakwater using UAVs and photogrammetry," *Procedia Structural Integrity*, vol. 37, pp. 167–172, 2022.

[39] H. Kim, J. Yoon, and S.-H. Sim, "Automated bridge component recognition from point clouds using deep learning," *Structural Control and Health Monitoring*, vol. 27, no. 9, Article ID e2591, 2020.

[40] C. Yi, D. Lu, Q. Xie, J. Xu, and J. Wang, "Tunnel deformation inspection via global spatial Axis extraction from 3D raw point cloud," *Sensors*, vol. 20, no. 23, p. 6815, 2020.

[41] F. Hamid-Lakzaeian, "Point cloud segmentation and classification of structural elements in multi-planar masonry building facades," *Automation in Construction*, vol. 118, Article ID 103232, 2020.

[42] P. S. Dabrowski, "Novel PCSE-based approach of inclined structures geometry analysis on the example of the Leaning Tower of Pisa," *Measurement*, vol. 189, Article ID 110462, 2022.

[43] Z. Zhou and J. Gong, "Automated analysis of mobile LiDAR data for component-level damage assessment of building structures during large coastal storm events," *Computer-Aided Civil and Infrastructure Engineering*, vol. 33, no. 5, pp. 373–392, 2018.

[44] R. Yu, P. Li, J. Shan, and H. Zhu, "Structural state estimation of earthquake-damaged building structures by using UAV photogrammetry and point cloud segmentation," *Measurement*, vol. 202, Article ID 111858, 2022.

[45] K. Dai, A. Li, H. Zhang, S. E. Chen, and Y. Pan, "Surface damage quantification of postearthquake building based on terrestrial laser scan data," *Structural Control and Health Monitoring*, vol. 25, no. 8, Article ID e2210, 2018.

[46] B. Xu and C. Liu, "A 3D reconstruction method for buildings based on monocular vision," *Computer-Aided Civil and Infrastructure Engineering*, vol. 37, no. 3, pp. 354–369, 2022.

[47] P. Martínez-Carricondo, F. Agüera-Vega, F. Carvajal-Ramírez, F. J. Mesas-Carrascosa, A. García-Ferrer, and F. J. Pérez-Porras, "Assessment of UAV-photogrammetric mapping accuracy based on variation of ground control points," *International Journal of Applied Earth Observation and Geoinformation*, vol. 72, pp. 1–10, 2018.

[48] E. Sanz-Ablanedo, J. H. Chandler, J. Rodríguez-Pérez, and C. Ordóñez, "Accuracy of unmanned aerial vehicle (UAV) and SfM photogrammetry survey as a function of the number and location of ground control points used," *Remote Sensing*, vol. 10, no. 10, p. 1606, 2018.

[49] O. Tziavou, S. Pytharouli, and J. Souter, "Unmanned Aerial Vehicle (UAV) based mapping in engineering geological surveys: considerations for optimum results," *Engineering Geology*, vol. 232, pp. 12–21, 2018.

[50] M. W. Smith, J. L. Carrivick, and D. J. Quincey, "Structure from motion photogrammetry in physical geography," *Progress in Physical Geography: Earth and Environment*, vol. 40, no. 2, pp. 247–275, 2016.

[51] E. I. Jeon, S. J. Yu, H. W. Seok, S. J. Kang, K. Y. Lee, and O. S. Kwon, "Comparative evaluation of commercial softwares in UAV imagery for cultural heritage recording: case study for traditional building in South Korea," *Spatial Information Research*, vol. 25, no. 5, pp. 701–712, 2017.

[52] V. Casella, F. Chiabrando, M. Franzini, and A. M. Manzino, "Accuracy assessment of a UAV block by different software packages, processing schemes and validation strategies," *ISPRS International Journal of Geo-Information*, vol. 9, no. 3, p. 164, 2020.

[53] I. Elkhrachy, "Accuracy assessment of low-cost unmanned aerial vehicle (UAV) photogrammetry," *Alexandria Engineering Journal*, vol. 60, no. 6, pp. 5579–5590, 2021.

[54] S. Jiang, C. Jiang, and W. Jiang, "Efficient structure from motion for large-scale UAV images: a review and a comparison of SfM tools," *ISPRS Journal of Photogrammetry and Remote Sensing*, vol. 167, pp. 230–251, 2020.

[55] S. Kameyama and K. Sugiura, "Effects of differences in structure from motion software on image processing of unmanned aerial vehicle photography and estimation of crown area and tree height in forests," *Remote Sensing*, vol. 13, no. 4, p. 626, 2021.

[56] E. Alexiou and T. Ebrahimi, "On subjective and objective quality evaluation of point cloud geometry," in *Proceedings of the 2017 Ninth International Conference on Quality of Multimedia Experience (qomex)*, pp. 1–3, Erfurt, Germany, June 2017.

[57] Federal Emergency Management Agency (Fema), "Seismic Performance Assessment of Buildings," *Methodology*, Vol. 1, Federal Emergency Management Agency, Washington, DC, USA, 2018.